Southward recirculation of the East China Sea Kuroshio west of Okinawa Island

Yukiharu Hisaki[1] and Chika Imadu[1,2]

[1]   The surface current of the Kuroshio recirculation region in the East China Sea is investigated. The surface currents in the west of Okinawa Island observed by HF radars and the assimilation results of the Japan Coastal Ocean Predictability Experiment (JCOPE) are analyzed. It appeared that currents in the easternmost edge of the Kuroshio bifurcate southward and flow into the west of Okinawa Island from JCOPE data. The currents are called Kuroshio southward recirculation currents. The currents are controlled by the bottom topography. The wind stress curl in the area where the bifurcated current can be seen in JCOPE data is negative, while the curl is positive in the eastern portion of the Kuroshio. The Kuroshio southward recirculation currents are sometimes enhanced, and their enhancement coincides with that of the positive and negative wind stress curls.

1.   Introduction

[2]   Western boundary currents such as the Kuroshio and Gulf Stream often affect the coastal areas west of the currents. There are studies that observed the coastal areas west of the Kuroshio. For example, temporal enhancement of the surface current from the Kuroshio region to the coast is observed [e.g., *Takeoka et al.*, 1995; *Hinata et al.*, 2005]. On the other hand, studies that observed the coastal currents in the recirculation region east of the Kuroshio are scarce.

[3]   The Okinawa Island is located east of the Kuroshio, and the waters west of Okinawa Island may be affected by it (Figure 1). However, observational studies of the physical oceanography west of Okinawa Island are quite a few and limited to the sea surface temperature (SST) [*Nadaoka et al.*, 2001; *Yanagi et al.*, 2002], with the exception. One of the exceptions is the hydrographic observation along PN line by Japan Meteorological Agency (JMA).

[4]   Hydrographic data have been observed quarterly by the JMA along the PN line across the Kuroshio in the central East China Sea (ECS) from 30°N, 124.5°E to 27.5°N, 128.25°E over 30 years. The surface geostrophic velocity across the PN line shows a southwest geostrophic velocity component to the east of the Kuroshio [e.g., *Yuan et al.*, 1994; *Oka and Kawabe*, 1998; *Liu and Yuan*, 1999].

[5]   *Nitani* [1972] suggested the presence of the southwestward currents in this region from shipboard GEK and hydrographic data. However, the current data are scarce, and the surface current field in this area is not well known. In fact, the presence of the southwestward currents in this area cannot be seen in surface mean currents in the ECS derived from GEK data by *Qiu and Imasato* [1990]. The previous studies have only shown the southwestward current component in the region. The questions raised here are as follows: How is the spatial variability of the current field to the east of the Kuroshio in the west of the Okinawa and its relationship with bottom topography? How is the temporal variability of the current field in this area and its relationship with other atmospheric or oceanic variables? Continuous observation of ocean currents at various points is required to reveal the temporal and spatial variability of the current field in this area.

[6]   The objective of the study was to reveal the surface current field west of Okinawa Island, and to consider its relation to both the Kuroshio and the wind field. We analyzed ocean surface currents observed by HF ocean radars. HF ocean radar is used to measure ocean surface currents [e.g., *Barrick et al.*, 1977; *Prandle and Ryder*, 1985; *Takeoka et al.*, 1995; *Hisaki et al.*, 2001; *Hisaki and Naruke*, 2003] and surface waves [e.g., *Hisaki*, 1996, 2002, 2004, 2005, 2006] over broad spatial areas. The method is to radiate high-frequency radio waves and analyze the backscattered signals from the ocean. HF ocean radar is useful to investigate the spatial variability of the surface currents. For example, *Takeoka et al.* [1995] was the first to use HF ocean radars to detect intrusion of the western boundary current (Kuroshio). The intrusion of the Gulf Stream has also been detected by HF radars [*Marmorino et al.*, 1998].

[7]   In section 2, we describe the observations by HF radars, in situ data, and other remotely sensed data. The Japan Coastal Ocean Predictability Experiment (JCOPE)

---

[1]Department of Physics and Earth Sciences, University of the Ryukyus, Nishihara, Japan.
[2]Now at Seiki, Kyoto, Japan.
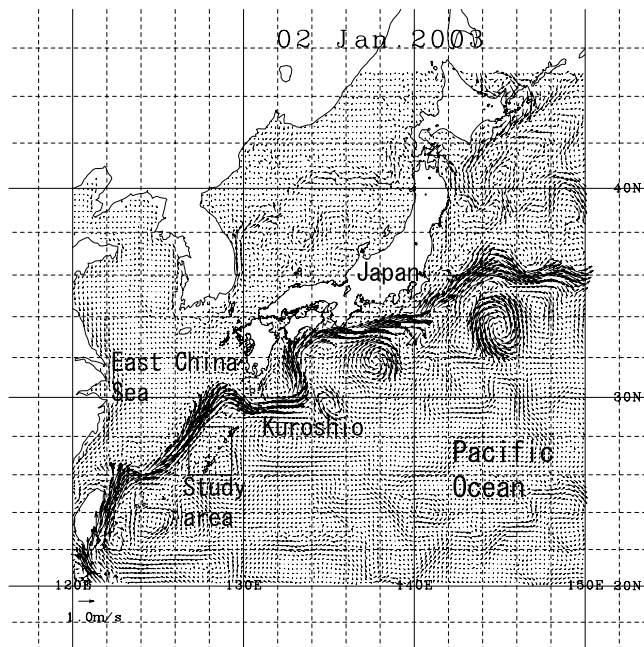
Figure 1. Study area and JCOPE surface currents (section 2.2) on 2 January 2003.

assimilation data are also described in section 2. The results from HF radars, in situ data, and other remotely sensed data are presented in section 3, and an analysis of the assimilated data is presented in section 4. A possible scenario for the results is presented in section 5. Section 6 presents our conclusions.

2. Observation

2.1. HF Ocean Radar

[8] Surface currents observed by HF ocean radars were obtained from May to July in 1999, and October to December in 1999. The HF ocean radars of Okinawa Radio Observatory, Communications Research Laboratory (Okinawa Subtropical Environment Remote-Sensing Center, National Institute of Information and Communications Technology) were deployed along the west coast of Okinawa Island. The radio frequency was 24.5 MHz. The radial velocities are sampled on polar grid points with the origin at the radar position. The temporal resolution of the radar system is 2 h. The radar was of the beam-forming type, with the beam forming electronically controlled by a phase shifter in real time. The beam step was 7.5°. The range resolution of the radar was 1.5 km. The currents were spatially and temporally interpolated to 1.5 km regular grid points. Details of the HF ocean radar system are described by *Hisaki et al.* [2001].

[9] The radars were located at site A (26° 22′ 48″N, 127° 43′ 49″E) and site B (26° 09′ 40″N, 127° 39′ 18″E) in 1999 (Figure 2a). The radars were located at site A (26° 34′ 34″N, 127° 13′ 11″E) and site B (26° 22′ 48″N, 127° 43′ 49″E) in 2000 (Figure 2b). Site A in 2000 (Figure 2b) is on Aguni Island, while other radar sites are on Okinawa Island. In 1999 the beam directions were from 193.5°T to 283.5°T for radar A and from 240°T to 330°T for radar B with a 7.5°

step. In 2000 the beam directions were from 129.5°T to 212°T for radar A and from 199°T to 281.5°T for radar B.

[10] The analysis periods were from 25 May to 8 July in 1999 and 10 October to 20 November in 2000. Some data are missing because of troubles with the radar system. For example, there were no data collected from 2 JST 27 May to 16 JST 27 May in 1999 and from 22 JST 27 October to 18 JST 30 October in 2000.

[11] The HF radar-estimated currents were compared with the currents measured by the current meter described by *Hisaki et al.* [2001]. The correlation coefficients were greater than 0.85 and the root-mean-square difference of velocity components between the sensors was about 10 cm s^{-1} [*Hisaki et al.*, 2001]. Therefore, we can consider that the HF ocean radar-estimated currents are sufficiently accurate for our purposes. The results from HF radar observations were also confirmed by the data assimilation results.

2.2. Other Data

[12] We also used daily averaged SST data from the TRMM (Tropical Rainfall Measurement Mission) Microwave Imager. The spatial resolution of SST from the TMI (TRMM Microwave Imager) was 0.25° × 0.25° [e.g., *Shibata et al.*, 1999]. The TMI SST data had less degradation from clouds than the NOAA/AVHRR SST data. The TMI SST data was compared with that from in situ observations. The correlation was about 0.98 and the root-mean-square difference between them was about 0.8°C [e.g., *Hisaki et al.*, 2001].

[13] The HF ocean radar observations are limited in both spatial coverage and period. We also used the data assimilation results of the Japan Coastal Ocean Predictability Experiment (JCOPE) from 2003 to 2005. The JCOPE data from 1999 and 2000 are unavailable. Altimetric surface heights, SST from satellites and in situ observation data from GTSPP (Global Temperature-Salinity Profile Program, available at http://www.nodc.noaa.gov/GTSPP/gtspp-home.html) are incorporated into the assimilation system. A summary of the assimilation method is given by *Miyazawa and Yamagata* [2003] (available at http://www.jamstec.go.jp/frcgc/jcope/htdocs/jcope_system_description.html).

[14] The horizontal resolution was 1/12° with 45 sigma levels. The ocean model is based on the Princeton Ocean Model (POM). The ocean model is described by *Miyazawa et al.* [2004]. Incremental Analysis Updates (IAU) developed by *Bloom et al.* [1996] were used to incorporate the data into the model. The IAU analysis of the JCOPE data is done within a 7-day window, while the IAU analysis cycle of *Bloom et al.* [1996] is 6 h.

[15] The ocean data are created on grid points using optimal interpolation at 7-day intervals. The assimilation data prior to 3.5 days at the interpolation time were used as initial data. These data were obtained in the previous cycle of the IAU. The prognostic equations, which are based on the POM, were integrated over 3.5 days from the initial data. The differences between optimally interpolated data and model-predicted data were evaluated. The IAU forcing terms were estimated from the evaluated differences by dividing the IAU analysis cycle (7 days). The prognostic equations with the IAU forcing terms were integrated over
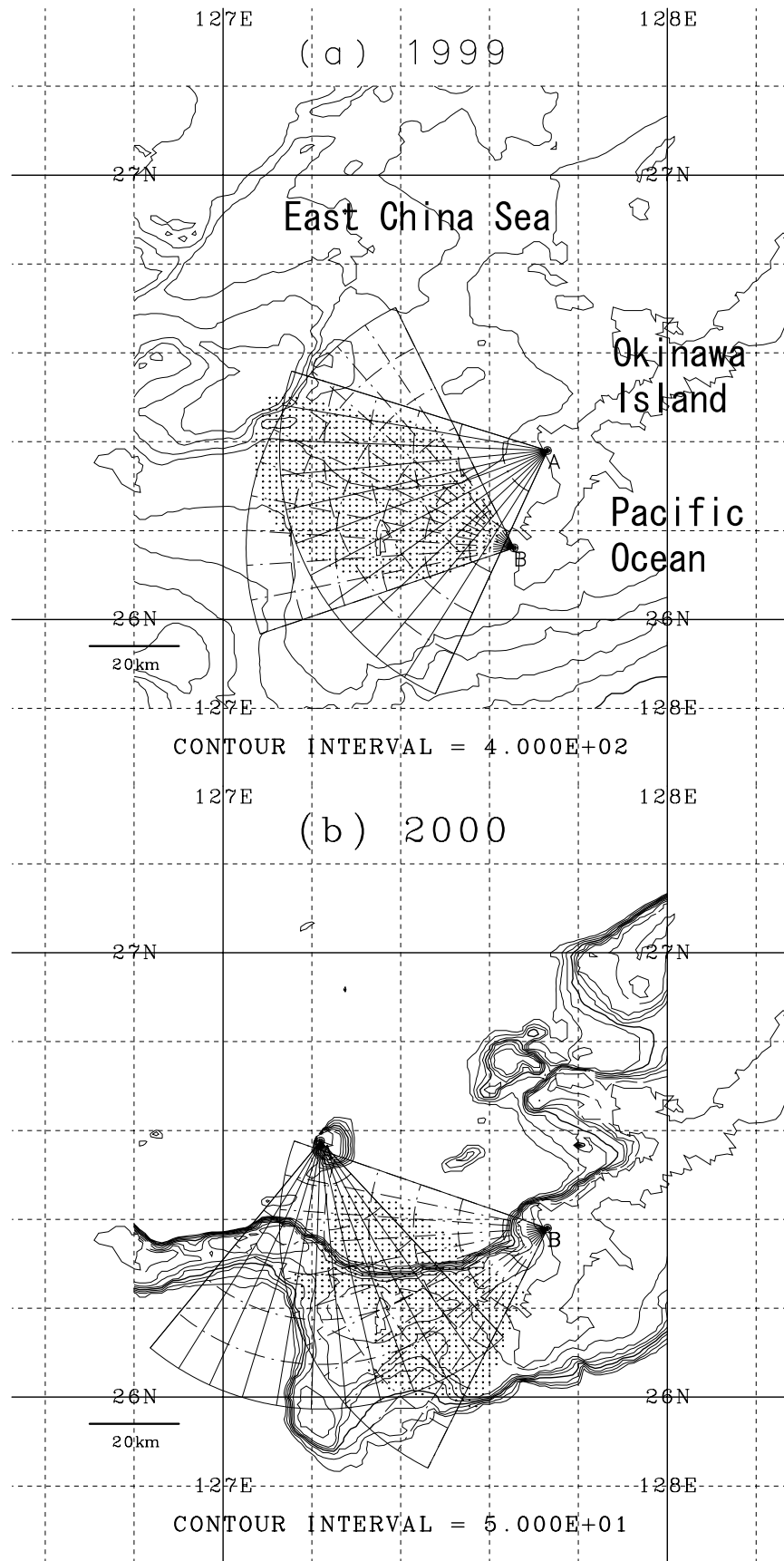
Figure 2. HF radar observation area for (a) 1999 and (b) 2000. Capital letters A and B indicate radar positions. Contour interval is 400 m in Figure 2a. Maximum depth contour is 400 m, and contour interval is 50 m in Figure 2b.

7 days from the initial data. Thus, the assimilation data in one IAU analysis cycle were obtained using the IAU.

[16] Small islands such as Aguni Island (radar site A in 2000) and Tokashiki Island (26.2°N, 127.35°E) near Okinawa Island are not well resolved. The temporal resolution of the supplied data was 2 days. The total area of the HF radar data is a few points effectively in terms of JCOPE data points. Both the HF radar data and the JCOPE data are spatially averaged data. The scale of the averaging is the resolution of the data, and the averaging scale of HF radar data is different from that of the JCOPE data. Daily sea surface NASA's Quick Scatterometer (QuikSCAT) Level3 wind vectors data on $0.25° \times 0.25°$ grid points were also used for this study.

[17] The Maps of Sea Level Anomalies (MSLA) were estimated from altimetric data by ERS and TOPEX/POSEIDON, and were provided by the CLS Space Oceanography Division [*Collecte Localisation Satellites*, 2001] at 7-day intervals. The MSLA from altimetric data were estimated by removing the 7-year mean (January 1993 to January 1999), geoid heights, tidal height signals, and the effects of the inverse barometer. The MSLA are provided on Mercator 1/3° grids. The longitudinal resolution varies with the cosine of the latitude.

3. Observation Results

3.1. Surface Currents Observed by HF Radars

[18] Figures 3a and 3b show time-averaged current fields in the observation period of 1999 and 2000, respectively. The mean currents in the observation period of 1999 are southeastward (Figure 3a). The currents in the southern part of the observation area (south of 26.2°N) are directed more eastward. The mean currents in the observation period of 2000 are southwestward (Figure 3b). The magnitudes of the mean currents are the largest in the northeast part of the observation area. The spatially averaged magnitudes of the time-averaged currents are 12 cm s^{-1} in 1999 and 13 cm s^{-1} in 2000.

[19] Figures 4a and 4b show area-averaged daily surface currents in the area of 26.25–26.5°N and 127.22–127.63°E. The currents were eastward or southeastward throughout most of the 1999 HF radar observation period.

[20] The southeastward current speeds are large from 7 to 13 June to in 1999 (Figure 4a). The maximum area-averaged daily current was observed on 8 June, but the daily averaged wind speed was not the maximum on that day. The currents were southwestward throughout most of the 2000 HF radar observation period. The area-averaged daily current speed was the largest on 1 November in 2000, and the daily averaged wind speed was also largest on that day. However, the wind directions were northwestward on 1 November in 2000. The area-averaged daily currents are time variable; however, northward currents are rare.

3.2. SST Data

[21] The along-isotherm components of ocean currents are generally larger than the cross-isotherm components on the basis of the thermal wind relationship, if the geostrophy is well satisfied [e.g., *Kelly*, 1989; *Zavialov et al.*, 2005]. The ocean currents are generally almost parallel to isotherms.

[22] Figures 4c and 4d show time series of rotated SST gradient vectors. The rotated SST gradient vector is the 90° counterclockwise rotation of the SST gradient vector. The rotated SST gradient vector is parallel to the isotherm with high temperature to the right, and parallel to the along-isotherm component of the current. The SST gradients were calculated by the least squares method in the area of 127–128°E and 26–28°N. However, the SST was not estimated in the area of 26–27°N, and 127.5–128°E, and the SST gradients were estimated in the remaining area.

[23] The SST gradients were estimated by solving the overdetermined equations as

$$T(x,y) = ax + by + c, \qquad (1)$$

where (x, y) is the horizontal coordinate, $T = T(x, y)$ is the SST at (x, y), and (a, b, c) is the unknown to be estimated. The rotated SST gradient vector is $(-b, a)$.

[24] The mean magnitude of the SST gradient from 25 May to 10 July in 1999 was 1.2×10^{-2} deg km^{-1}. The mean magnitude from 18 October to 22 November in 2000 was 6.8×10^{-3} deg km^{-1}. The direction of the rotated SST gradients is almost southward. It is rare that the rotated SST gradient is directed northward. The rotated SST gradient vectors are related with area-averaged daily currents from Figures 4c and 4d and Figures 4a and 4b. However, area-averaged daily currents in 1999 are directed counterclockwise with respect to the rotated SST gradient vectors. This counterclockwise veering of surface currents with respect to the rotated SST gradient vectors can be seen in Figure 4a. A possible explanation of the veering in 1999 is that the southwesterly winds dominate in 1999, while northeasterly winds dominate in 2000.

[25] We estimated complex correlation coefficients between area-averaged daily currents and rotated SST gradient vectors, but there were no correlations. In the case of small magnitudes of area-averaged rotated SST gradients, isotherms were complicated in the area, and the horizontal variability of currents was large. The rms differences between area-averaged surface current directions and rotated SST gradient vectors of magnitudes greater than 0.01 deg km^{-1} were 73° in 1999 and 44° in 2000, respectively. The rms difference in 1999 was larger than that in 2000 because of the southerly winds in 1999.

3.3. Other Remotely Sensed Data

[26] Figure 5a shows the mean wind vectors and wind stress curl from 18 October to 20 November in 2000. The derivatives of wind stress components are calculated by the centered difference. The wind stresses are calculated from daily wind vectors and the wind stresses are averaged. The time-averaged wind directions are southwestward. The wind directions near the HF ocean radar observation are also southwestward. The wind stress curl in the southeastern (northwestern) part of the area of 27–28°N and 127–128°E is negative (positive).

[27] Figure 5b shows the time-averaged wind vectors and wind stress curl during the periods when the southward currents were strong. The periods for the average were selected from Figure 4b: 25–27 October, 31 October,
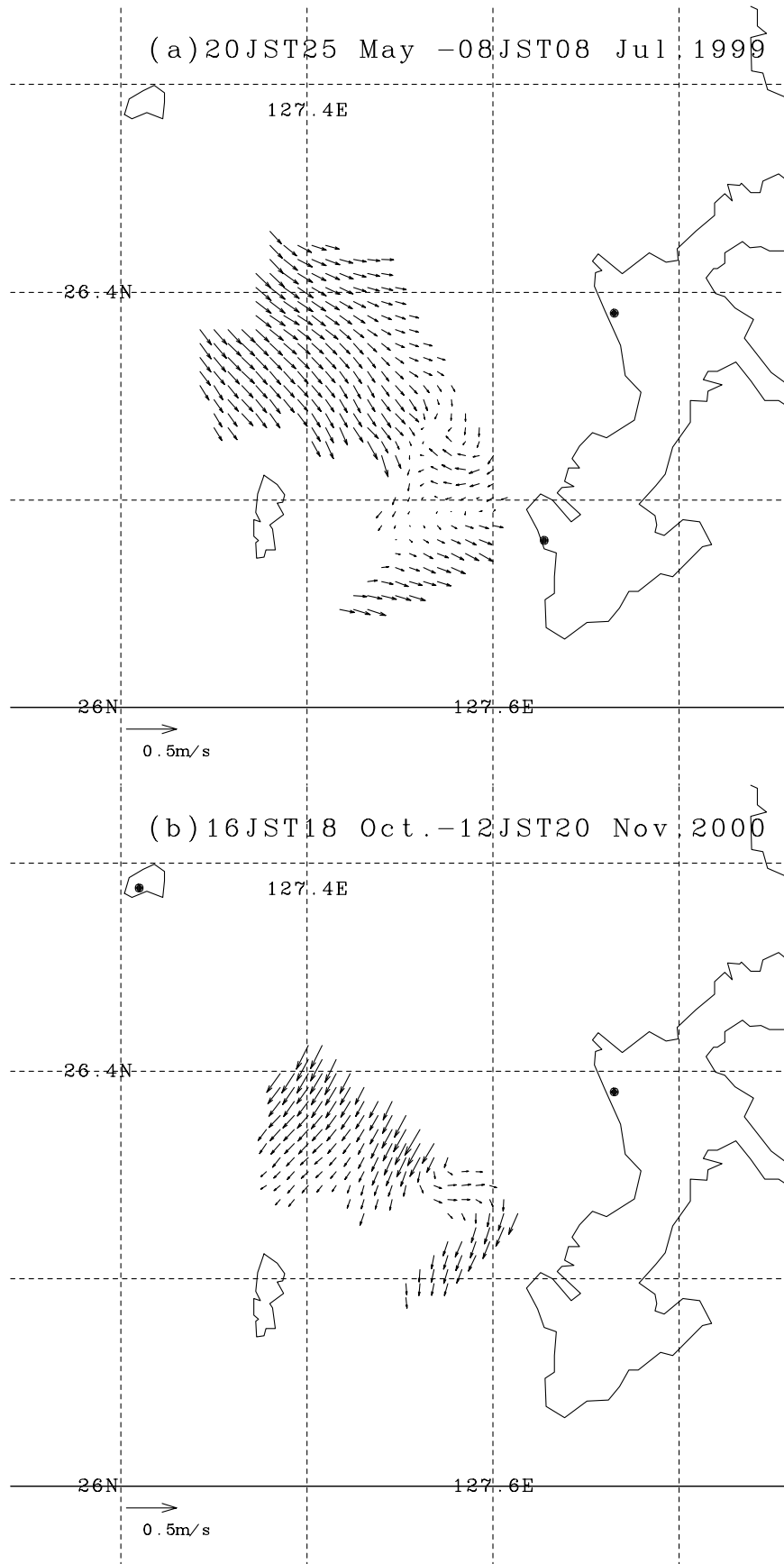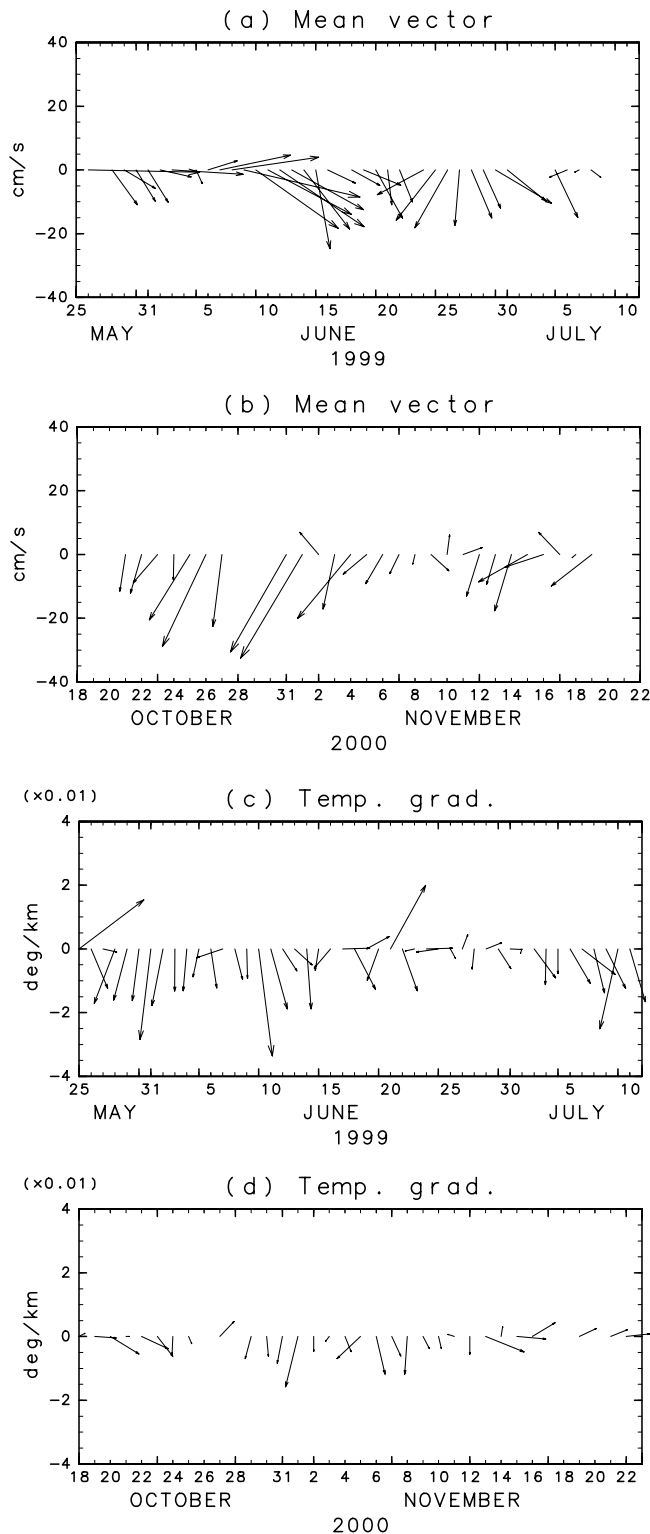
Figure 3. Time-averaged currents observed by HF radars in (a) 1999 and (b) 2000.

Figure 4. Area-averaged daily surface currents over 26.25–26.5°N and 127.22–127.63°E in (a) 1999 and (b) 2000. Time series of rotated SST gradient vectors in (c) 1999 and (d) 2000.

1 November, 3–4 November, and 20 November. Most of the mean wind directions in the East China Sea are southwestward. However, mean wind directions to the south of the HF radar observation area are westward or northwestward. The negative (positive) wind stress curl in the southeastern (northwestern) part of the area of 27–28°N and 127–128°E was enhanced in the selected periods.
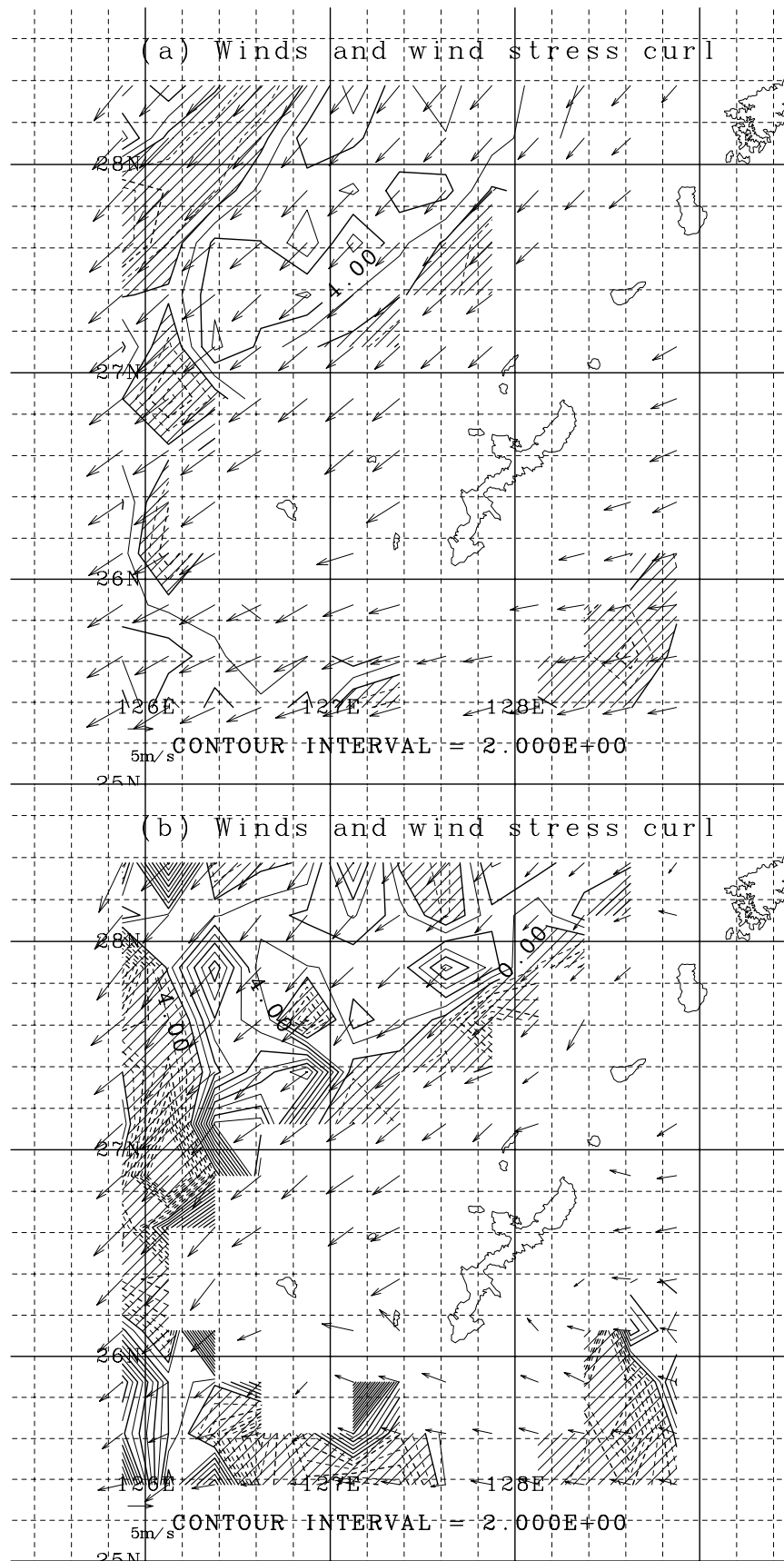
[28] Figure 6 is the HF radar observation period-averaged MSLA. While mesoscale eddies are dominant in the Pacific Ocean, mesoscale eddies are not so dominant in the East China Sea in Figure 6. A cyclonic eddy can be seen in the area of 24–26°N and 126–128°E (Figure 6a), where the SST is low. There are no significant eddies in the East China Sea in Figure 6a. The area of 24–26°N and 126–128°E is surrounded by cyclonic and anticyclonic eddies in Figure 6b. The magnitudes of the MSLA gradients are small to the west of Okinawa Island. It is shown that the effects of the mesoscale eddies on surface currents were small in the HF radar period-averaged current fields.

4. Analysis of JCOPE Data

4.1. General

[29] The surface currents observed by HF ocean radars are southward. We can expect that the eastern part of the Kuroshio veers southward from northeastward from the SST. We call it the Kuroshio southward recirculation current. We analyzed the JCOPE data to infer the beginning of the Kuroshio southward recirculation current. We investigated the mechanism of the current and found from the HF radar observations that the southward currents are sometimes enhanced. We investigated the environmental conditions when the southward current is strong from QuikScat wind data.

[30] Figure 7a is the 3-year mean surface currents ($\bar{\mathbf{v}} = (\bar{u}, \bar{v})$) of JCOPE data from 2003 to 2005, where $\bar{u}$ and $\bar{v}$ are the time-averaged east and north components, respectively. Figure 7b shows the mean surface currents of the JCOPE data when the southward current in the HF radar observation area was strong, as explained in section 4.2. The eastern part of Kuroshio veers southward, but the magnitude of the southward current near the eastern edge of Kuroshio is small. The southward currents are confluent with southwestward currents in the area 27.2–28°N and 127.8–128.2°E. The confluent currents flow into the area of 26.2–27°N and 127.2–127.6°E. On the other hand, the currents off the western part of the Kuroshio are almost parallel to the Kuroshio. The Kuroshio southward recirculation current can be seen only off the eastern part of the Kuroshio in the area of Figure 7a. The spatially averaged magnitude of mean currents in the area of 26.1–26.5°N and 127.2–127.6°E is 7.4 cm s^{-1}, which is consistent with the result of the HF radar observation, considering the difference of water depth of surface currents. The JCOPE surface current is the mean current in the upper 10 m layer, while the HF ocean radar current is the current at several tens of centimeters. We can infer that the surface current observed by HF radars is the Kuroshio southward bifurcation. Because mean currents are quite weak in the study area, the temporal variability of currents is shown. The confidence intervals of mean currents are also estimated.

Figure 5. Mean wind vectors and wind stress curl (in 10^{-7} N $\times$ m^{-3}) by QuikScat data during (a) the 2000 HF radar observation period and (b) the 2000 HF radar observation period when the southward currents were strong. The shaded areas indicate negative values.
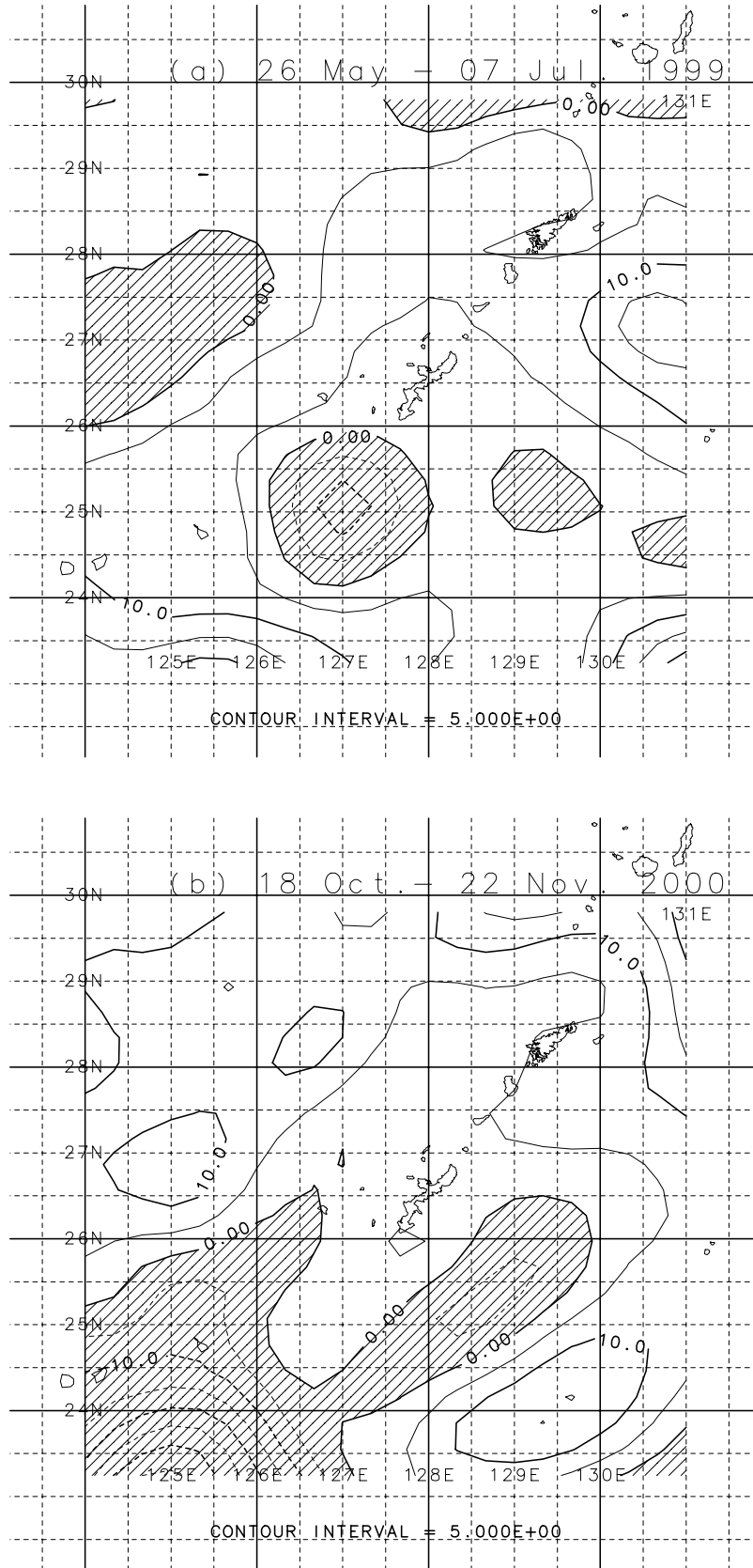
Figure 6. HF radar observation period-averaged MSLA in (a) 1999 and (b) 2000. The shaded areas indicate negative values.
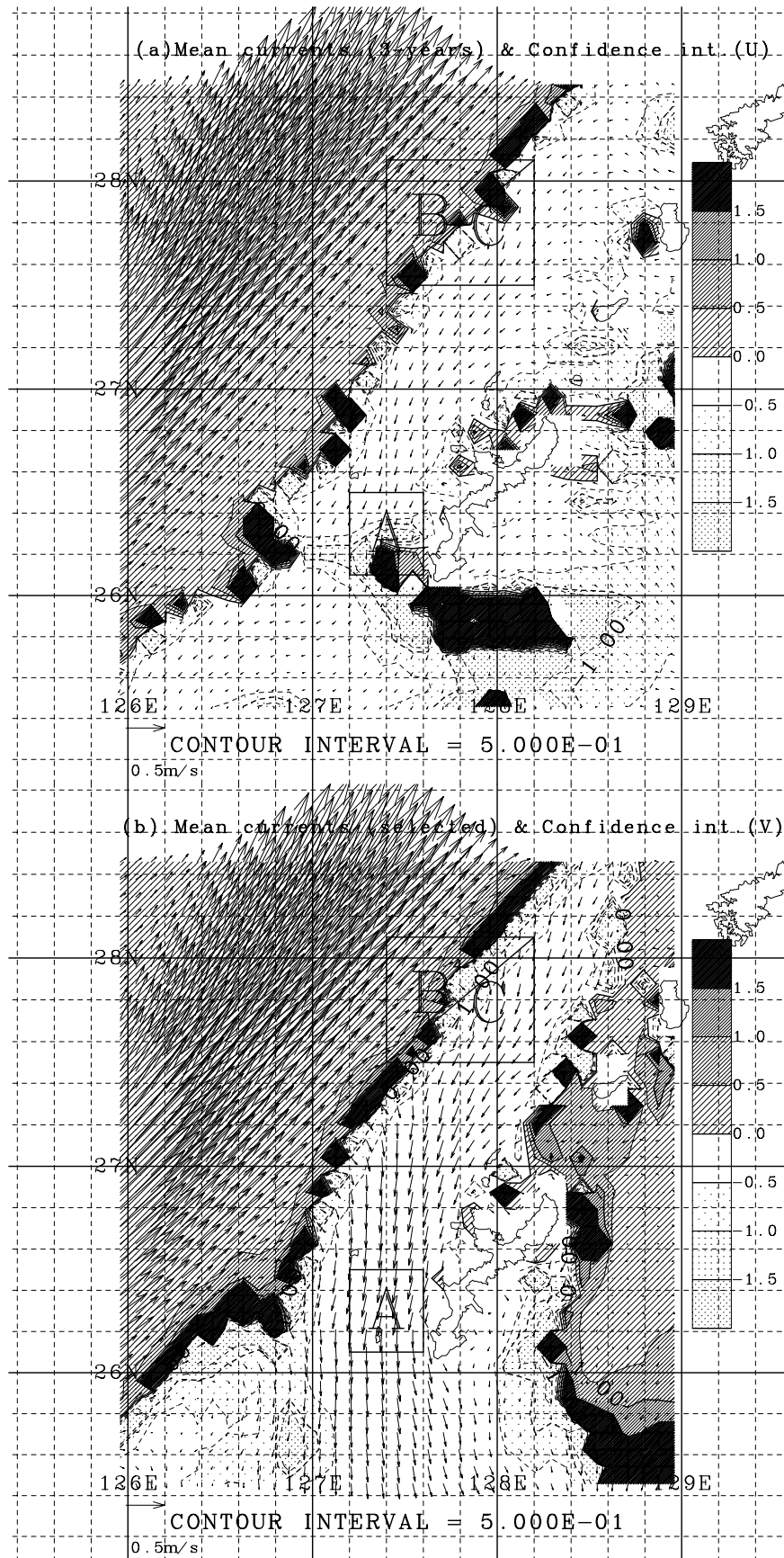
Figure 7

4.2. Enhancement of the Southward Current

[31] The southward current is sometimes enhanced as shown in section 3 (Figures 4a and 4b). The enhancement of the current is also seen in JCOPE data.

[32] We selected periods when the southward currents were strong from the JCOPE surface current vector maps from 2003 to 2005. Figure 7b shows the mean surface currents for those selected periods. The selected periods in 2003 were 2–10 April, 6–8 May, 15–19 July, 26–30 August, and 5–15 October. The periods in 2004 were 14–16 April, 21–23 June, 5–13 July, 31 July to 10 August, and 13–17 October. The periods in 2005 were 13–17 April, 7–10 May, 21–23 May, 12–29 June, 4–12 July, 22 July to 4 August, 7–23 August, 6–8 September, 26–30 September, and 10–16 October. The current in the eastern part of the Kuroshio veers southwestward around the area of $27–28°N$ and $127–128°E$ in Figure 7b, then flows into the HF radar observation area. The spatially averaged magnitude of mean currents in the area of $26.1–26.5°N$ and $127.2–127.6°E$ is 24.0 cm s^{-1}, which is about 3.2 times the 3-year mean current magnitude. The current directions for the selected period mean (Figure 7b) are similar to those of 3-year mean (Figure 7a).

4.3. Statistical Analysis

[33] The confidence intervals $\Delta_c(\bar{u}, p)$ and $\Delta_c(\bar{v}, p)$ of the 3-year mean currents were estimated, where p is the confidence level. The method to estimate degree of freedom is presented in Appendix A. Figure 7 shows the 90% confidence intervals of the mean east and north components normalized by mean values. For example, if $-1 < \Delta_c(\bar{u}, 0.9)/\bar{u} \leq 0$, the probability that the east component of the mean current is westward is more than 95% $((1 + p)/2)$. The values of $\Delta_c(\bar{u}, 0.9)/\bar{u}$ and $\Delta_c(\bar{v}, 0.9)/\bar{v}$ are small $(0 < \Delta_c(\bar{u}, 0.9)/\bar{u} < 0.5$ and $0 < \Delta_c(\bar{v}, 0.9)/\bar{v} < 0.5)$ in the Kuroshio area. The values of $\Delta_c(\bar{u}, 0.9)/\bar{u}$ and $\Delta_c(\bar{v}, 0.9)/\bar{v}$ are large along the eastern edge of Kuroshio. The values of $\Delta_c(\bar{u}, 0.9)/\bar{u}$ and $\Delta_c(\bar{v}, 0.9)/\bar{v}$ in the area of the recirculation current to the east of Kuroshio (around $27.5°N$, $128°E$) are $-0.5 < \Delta_c(\bar{u}, 0.9)/\bar{u} < 0$ and $-0.5 < \Delta_c(\bar{v}, 0.9)/\bar{v} < 0$. The values of degrees of freedom are greater than 100 in the area, but they are highly variable in the individual grid points. We can confirm that the mean currents in the area are southwestward with a high probability.

4.4. Time Series Data

[34] Figure 8 shows time series of the area-averaged JCOPE surface currents. The averaged area is $26.1–26.5°N$ and $127.2–127.6°E$, which is almost same as the HF radar observation area, and triangles B and C in Figure 7, which are close to the boundary between the Kuroshio and the recirculation currents.

[35] Most of the current directions are southward, and cases of northward currents are very few in Figure 8a. The time-averaged current of those area-averaged currents is $(\bar{u}, \bar{v}) = (-1.47, -7.03)$ (cm s^{-1}). The confidence interval at the

90% confidence level of $(\Delta_c(\bar{u}, 0.9), \Delta_c(\bar{v}, 0.9)) = (1.06, 1.03)$ (cm s^{-1}), and the degree of freedom is (141.9, 312.8). These southward current directions are consistent with Figures 4a and 4b. The northward currents in early and mid-September in 2003 are associated with the passage of Typhoon Maemi to the south and west of Okinawa Island.

[36] The currents are northeastward in Figure 8b. The time-averaged current of those area-averaged currents is $(\bar{u}, \bar{v}) = (13.5, 13.3)$ (cm s^{-1}). The confidence interval at the 90% confidence level is $(\Delta_c(\bar{u}, 0.9), \Delta_c(\bar{v}, 0.9)) = (2.05, 3.64)$ (cm s^{-1}), and the degree of freedom is (115.4, 45.9). The temporary variability of the area-averaged currents in area B (Figure 7) is associated with the position change of the Kuroshio edge.

[37] The currents in area C (Figure 7) are southward, which suggests that one of the beginnings of the currents in area A or the HF radar observation area is near the eastern edge of Kuroshio north of area A. The time-averaged current of those area-averaged currents is $(\bar{u}, \bar{v}) = (-0.63, -2.74)$ (cm s^{-1}). The confidence interval at the 90% confidence level is $(\Delta_c(\bar{u}, 0.9), \Delta_c(\bar{v}, 0.9)) = (1.07, 2.60)$ (cm s^{-1}), and the degree of freedom is (172.5, 40.3). The probability that the time-averaged current in area C is southward is more than 95%.

4.5. Bottom Topography and Potential Vorticity

[38] The factors contributing to the Kuroshio southward recirculation current are bottom topography, wind stress and stratification. Figure 9a is the contour map of the bottom topography (H). The JCOPE water depth data with $1/12°$ is used to draw Figure 9a.

[39] The path of the Kuroshio follows the slope from $(27.4°N, 126°E)$ to $(28.4°N, 127°E)$ in Figure 9a. The water depth of the Kuroshio is from 200 to 1000 m in this area. The water depth becomes shallower with the distance offshore from the western part of the Kuroshio.

[40] The bottom contour line $H = 1200$ m follows a path from $(27°N, 126°E)$ in Figure 9a to $(28°N, 127.5°E)$, and is then deflected southwestward. The currents change their directions in the area of $26.5–27.5°N$ and $127–127.5°E$. The currents flow southwestward along the contour of $H = 800$ m.

[41] The relative vorticity is much smaller than the planetary vorticity f except the Kuroshio area, and contour patterns of the potential vorticity for vertical homogeneous density fluids are similar to those of the bottom topography. The current direction follows the H contour line as a first approximation. The water depth of the southward current is from 400 to 800 m in this area.

[42] The currents also flow along the contour of $H = 800$ m in the area of $27–28°N$ and $127–128°E$ (Figures 7a and 9a). The contour of $H = 800$ m in the area of $27–28°N$ and $126–127°E$ is the path of the Kuroshio.

[43] The current field is affected by the topography. However, the surface currents in the area of $26–26.5°N$ and $127–127.6°E$ near Okinawa Island in Figure 7a do not

---

Figure 7. (a) Mean surface currents $(\bar{\mathbf{v}} = (\bar{u}, \bar{v}))$ of JCOPE data from the 3-year period from 2003 to 2005 overlaid by normalized confidence intervals of $\bar{u}$ at the 90% confidence level $(\Delta_c(\bar{u}, 0.9)/\bar{u})$. (b) Same as Figure 7a but for the periods when the southward current in the HF radar observation area was strong. The normalized confidence intervals of $\bar{v}$ (3-year mean) at the 90% confidence level are overlaid. The areas A, B, and C are averaging areas for Figure 8.
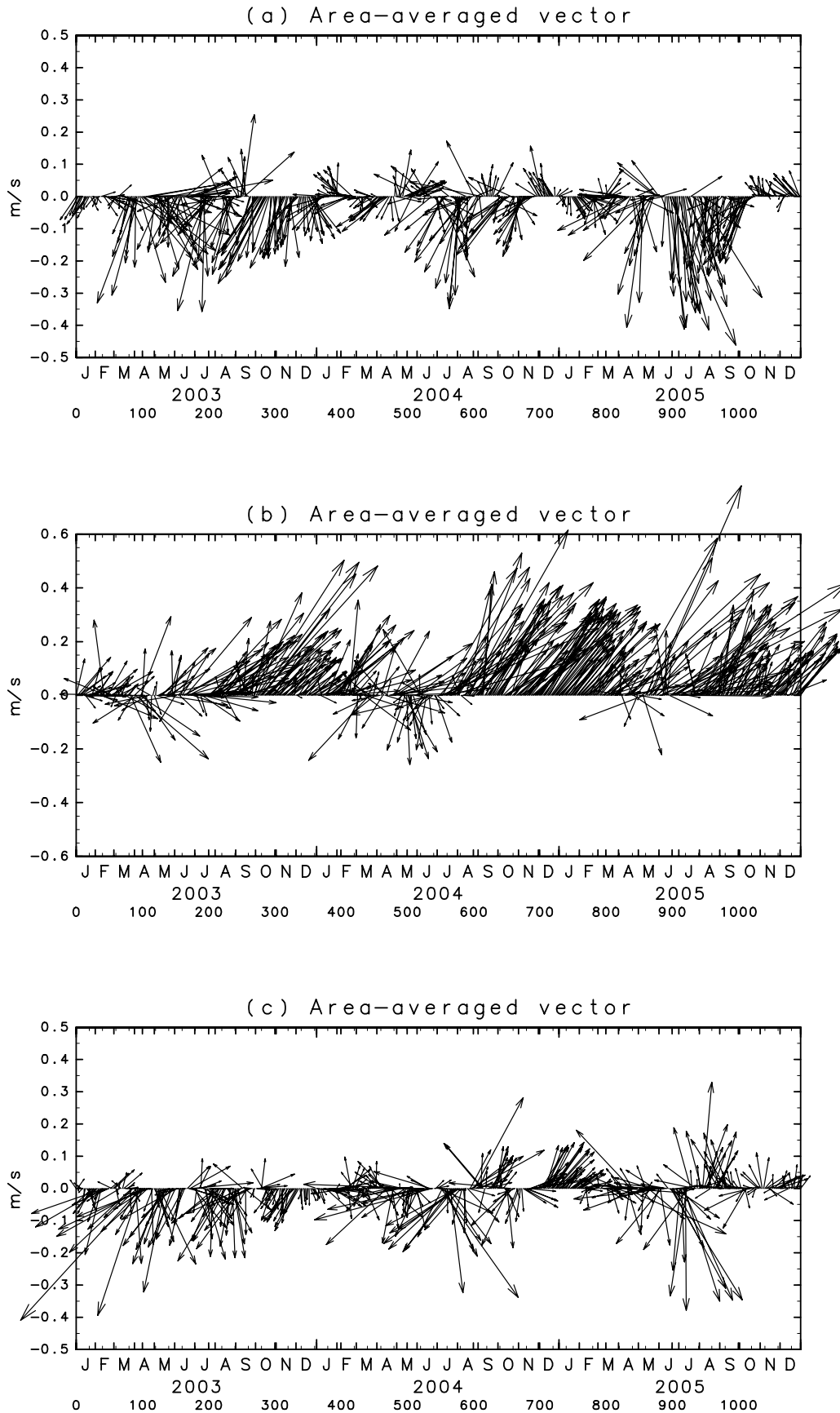
Figure 8

flow along the closed H contour lines in the area (Figure 9a). The numerical simulation by *Guo et al.* [2003] shows that this is due to JEBAR (joint effect of baroclinicity and bottom relief) effects. The current directions around the area of 28°N and 127.2°E, which is the eastern part of the Kuroshio, also diverge from the $H = 1200$ m contour line. The spatial variability of H is not large in this area.

[44] In the absence of external forces and dissipation, the Ertel's potential vorticity (EPV) is conserved following the water particles. The relationship between the EPV and the bottom topography is investigated. Figure 9b shows the contour map of the EPV at the 21.5 m depth. The EPV is approximated as

$$Q \simeq \frac{1}{\rho}\left[-\frac{\partial v}{\partial z}\frac{\partial \rho}{\partial x} + \frac{\partial u}{\partial z}\frac{\partial \rho}{\partial y} + (f + \zeta)\frac{\partial \rho}{\partial z}\right], \qquad (2)$$

where (u, v) is the current vector, ζ is the relative vorticity, and ρ is the sea water density. The horizontal component of the planetary vorticity vector and vertical component of the current are neglected in equation (2). The current flows along the EPV contour line in Figure 9b. The EPV contour patterns are similar to H contour lines in the area of 26–28°N and 127–128°E. The EPV contour patterns are more related with current directions than H contours. The current to the west of $Q = 3 \times 10^{-10}$ m^{-1} × s^{-1} contour line is the Kuroshio. The magnitudes of the EPV gradients are small in the Kuroshio area. The southwestward currents can be seen along the $Q = -6$ and $Q = -7 \times 10^{-10}$ m^{-1} × s^{-1} contour lines, where horizontal gradients of EPV are the largest in the area of 26–28°N and 127–128°E.

[45] If we can neglect the effects of stratification in this area, the results from the EPV are the same as those from the potential vorticity for vertical homogeneous density fluids, which is approximated as f/H in the area where the relative vorticity is much smaller than f. The result that the southward current flows both along the EPV contour and bottom topography shows that the southward current is controlled by bottom steering effect.

4.6. Sea Surface Wind

[46] Figure 10c shows the 3-year mean wind vectors and a contour map of the 3-year mean wind stress curl from QuikScat data. The mean wind direction is southwestward, and the Ekman transport is northwestward.

[47] We see the area of 27–28°N and 126–128°E in Figures 7a and 10c. The wind stress curl is negative in the western part of the Kuroshio, and increases from west to east. The local maximum of the wind stress curl in Figure 10c is at (27.4°N, 126.6°E), then decreases from west to east. The wind stress curl is negative off the eastern part of the Kuroshio (around 28°N, 128°E). The wind stress curl is positive above the path of the Kuroshio, and is negative to both the east and west of the Kuroshio.

[48] Figure 10b shows the mean wind vectors of the selected periods and the contour map of the mean wind stress curl in the selected periods from QuikScat data.

General features in Figure 10b are the same as those in Figure 10a. The averaged wind directions are southward or southwestward. However, the vector-averaged wind magnitudes are smaller than those in Figure 10a, which shows that the wind directions are variable in the selected period. The wind stress curl is positive above the path of the Kuroshio, and negative to both the east and west of the Kuroshio. The wind directions are not always southward or southwestward even in the selected periods. For example, the wind directions from 15 to 19 July in 2003 are northeastward or northward. On the other hand, the wind stress curl is positive above the path of the Kuroshio, and negative to both the east and west of the Kuroshio during this period.

[49] Figure 10c is the comparison of the wind stress curl at the 28.125°N latitude line. The 3-year mean positive wind stress curl is the maximum at 127.125°E along this latitude line while the selected-period mean positive wind stress curl is the maximum at 127.375°E along the latitude line. The position of the maximum positive wind stress is in the eastern part of the Kuroshio. The maximum averaged wind stress curl for selected periods is larger than that for the 3-year mean. The wind stress curl is zero at 128°E along the latitude line for both the 3-year and the selected-period mean. The wind stress curl is negative east of this longitude along the 28.125°N latitude line. The negative wind stress curl is enhanced in the selected periods. Confidence intervals of the mean wind stress curl were estimated. The probability that the 3-year mean wind stress curl is positive is greater than 95% from 127.125°E to 127.625°E in Figure 10c, where the degree of freedom ranges from 618.1 to 783.6. The probabilities that the 3-year mean wind stress curl is negative are greater than 95% at 128.125°E and 128.375°E in Figure 10c, where the degrees of freedom are 379.5 and 692.4, respectively. The probabilities that the selected-period mean wind stress curl is positive are greater than 95% at 127.125°E and 127.375°E in Figure 10c, where the degrees of freedom are 59.8 and 93.6, respectively. The probabilities that the selected-period mean wind stress curl is negative are greater than 95% at 128.125°E and 128.375°E in Figure 10c, where the degrees of freedom are 118.8 and 71.0, respectively.

[50] Hypothesis tests were performed to determine whether there were statistical differences between the mean of wind stress curl of the 3-year mean and selected-period mean for various confidence levels p. The maximum confidence levels that differences in mean wind stress curl at 128.375°E, 127.375°E, 126.125°E, and 127.875°E are statistically significant are 98%, 89%, 84% and 76%, respectively, where the degrees of freedom are 83.3, 139.5, 277.7 and 165.0, respectively. We can confirm that the negative wind stress curl east of the Kuroshio is enhanced in the selected period at a high probability.

5. Discussion
5.1. Ekman Velocity

[51] The Ekman velocities at the surface are estimated from the QuikScat data to discuss the Kuroshio recirculation

---

Figure 8. Time series of area-averaged JCOPE surface currents in (a) area A in Figure 7 (26.1–26.5°N and 127.2–127.6°E), (b) area B in Figure 7 (triangle with apexes at 27.5°N, 127.4°E; 28.1°N, 127.4°E; and 28.1°N, 128.2°E), and (c) area C in Figure 7 (triangle with apexes at 27.5°N, 127.4°E; 27.5°N, 128.2°E; and 28.1°N, 128.2°E).
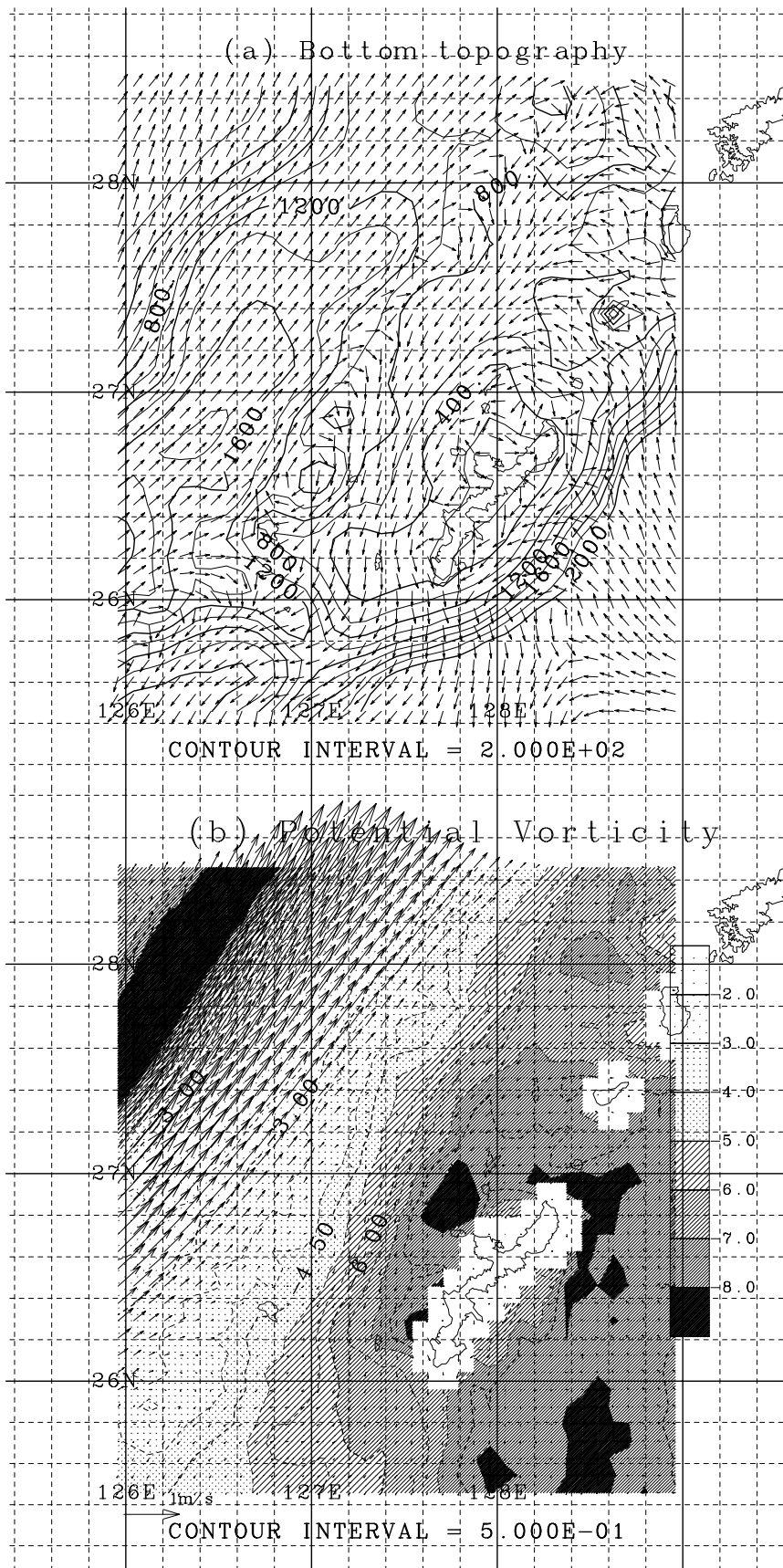
Figure 9. (a) Contour of water depth H overlaid by 3-year mean current directions (in m). (b) Contour map of the Ertel's potential vorticity Q (equation (2)) at the 21.5 m depth overlaid by 3-year mean currents at the 27.5 m depth (in 10^{-10} m^{-1} × s^{-1}).
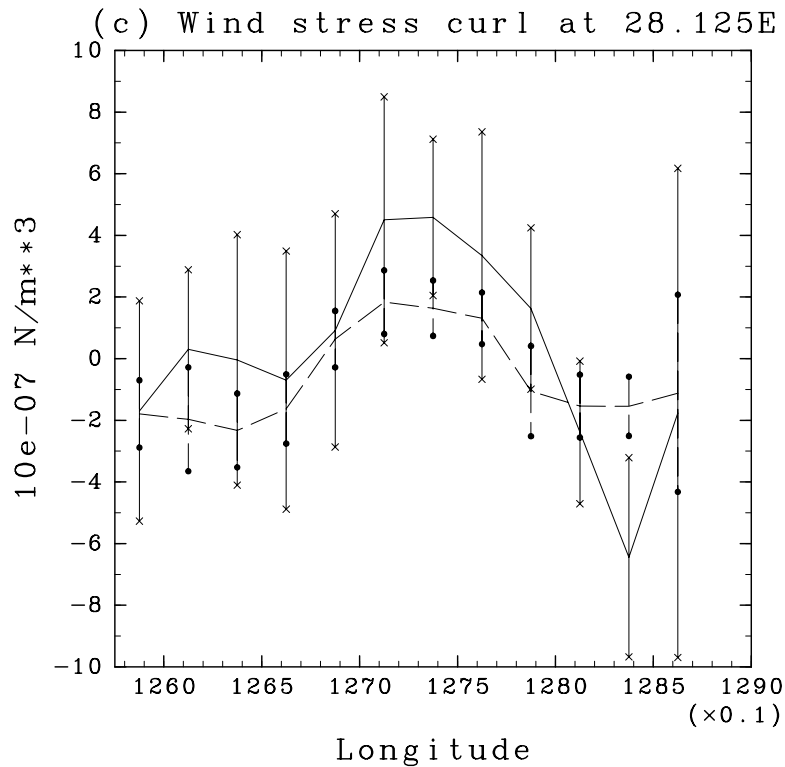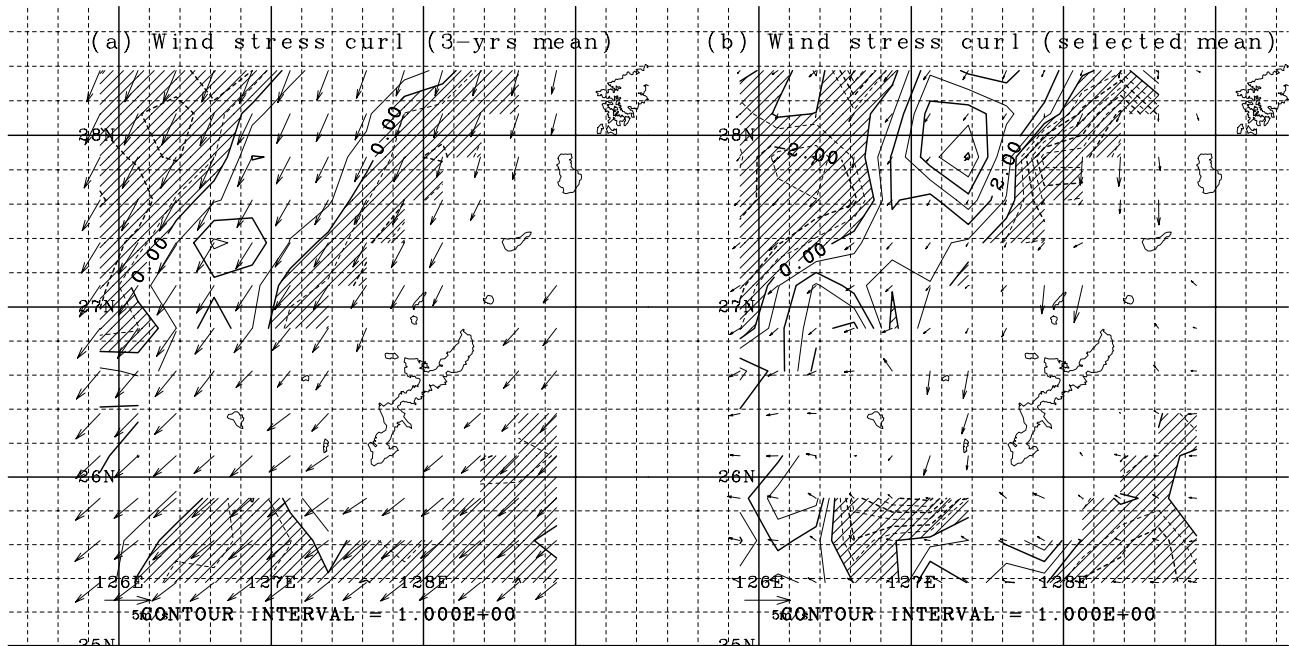
Figure 10. (a) Three-year mean wind vectors and contour map of the three-year mean wind stress curl (in 10^{-7} N $\times$ m^{-3}) from QuikScat data from 2003 to 2005. The shaded areas indicate negative values. (b) Same as in Figure 10a but for the selected period. (c) Three-year mean wind stress curl from 2003 to 2005 (dashed line) and mean wind stress curl for selected periods (solid line) along the 28.125°N latitude line. The crosses and black circles show confidence intervals of the selected period mean and 3-year mean wind stress curls at the 90% confidence interval, respectively.

itself and the surface current separately. The Ekman surface current in the complex form is

$$\mathbf{U}_E = \frac{2^{1/2}\boldsymbol{\tau}}{\rho f h_E} \exp\left(-i\frac{\pi}{4}\right) \exp\left(\frac{(1+i)}{h_e}z\right), \qquad (3)$$

where z is the vertical coordinate, $\boldsymbol{\tau}$ is the wind stress in the complex form, $h_e = (2A/f)^{1/2}$ is the Ekman depth, and A is the vertical momentum diffusivity.

[52] Figure 11 shows mean Ekman currents and the vertical current shears between the surface Ekman layer and the underlying water column for 3-year and the selected period. The Ekman depth is 27 m in this example, which is almost same as that of *Chereskin* [1995]. The surface current is composed of the geostrophic current and the Ekman current ($\mathbf{U}_g + \mathbf{U}_E$). The current beneath the Ekman layer is the geostrophic current ($\mathbf{U}_b$). The vertical current shear between the surface Ekman layer and the underlying water column is $\mathbf{U}_g + \mathbf{U}_E - \mathbf{U}_b$.

[53] If the Ekman velocity ($|\mathbf{U}_E|$) in the selected period is larger or comparable to the magnitude of vertical shear ($|\mathbf{U}_g + \mathbf{U}_E - \mathbf{U}_b|$), the current enhancement in the selected period is associated with the enhancement of the Ekman current. The depth of the Ekman current in Figures 11a and 11b is 5 m, because the thickness of the uppermost layer of the JCOPE data is 10 m. The depth of the current beneath the Ekman layer ($\mathbf{U}_b$) is πh_e. The shear vectors are plotted in the area of $H > 2\pi h_e$ (Figures 11c and 11d).

[54] The mean wind directions are southwestward (Figure 10a), and the Ekman current directions are westward. The 3-year mean Ekman currents are large, however, the selected mean Ekman currents are smaller than the vertical current shears (Figure 11). The enhancement of the southward current cannot be explained only by the enhancement of the surface Ekman velocities.

5.2. Wind Stress Curl and Current Enhancement

[55] This study shows that surface currents in the area between 26–28°N and to the east of the Kuroshio are southward, which is almost opposite to the direction of the Kuroshio. Analysis of HF radar observations and JCOPE data reveals that the southward currents are sometimes enhanced. The wind stress curl is positive above the eastern portion of the Kuroshio, while the curl is negative to the east of the Kuroshio. Positive wind stress curl is associated with high SST in the eastern part of the Kuroshio.

[56] This relation is a result of the local air-sea interaction along the Kuroshio SST front. The static stability of the atmospheric boundary layer is reduced, and the upward motion of the atmosphere in the boundary layer is enhanced. The horizontal wind is convergent [*Xie et al.*, 2002], and the relative vorticity of the wind field is positive. On the other hand, the boundary layer atmosphere to the east of the Kuroshio path is stable compared with that in the eastern part of the Kuroshio. The horizontal wind is divergent, and the relative vorticity of the wind stress field is negative [*Chelton et al.*, 2004].

[57] We used JCOPE data to investigate the vertical profile of the currents to the east of the Kuroshio and found that the currents are almost always southward. The transport vectors, which are estimated by integrating the currents with respect to the vertical coordinate, are also southward to the east of the Kuroshio. Existence of the Kuroshio southward recirculation current is primarily due to the bottom topography. The southward current is enhanced when the positive and negative wind stress curls are enhanced. The enhancement of currents occurs in surface waters.

[58] None of the selected periods, when the southward currents are enhanced, coincides with winter. Possibly, this is because southward monsoon winds from Asian continent are dominant in the study area during the winter. The atmospheric pressure is lower in the eastern part of the study area. The negative wind stress curl to the east of the Kuroshio and positive wind stress curl in the eastern portion of the Kuroshio are weakened during the winter, and the southward currents are not enhanced.

6. Conclusions

[59] We investigated the surface currents west of Okinawa Island, which is located to the east of the Kuroshio in the East China Sea. It was found that the time-averaged current field is almost southward, although the spatial variability of the current is affected by the topography. Because the HF radar observation period is not very long, the effect of the mesoscale eddy remained in the time-averaged current field. The area-averaged surface currents were also almost always southward, although there were temporal variabilities associated with the eddy field. The spatially averaged magnitudes of temporal mean currents are more than 10 cm s^{-1} in both HF radar observation periods.

[60] The southward currents are sometimes enhanced. The relationship of the enhancement was investigated using satellite remote sensing data. The QuikScat wind shows that the wind stress curl is negative (positive) in the southeastern (northwestern) part of the 27–28°E and 127–128°N area. The negative and positive wind stress curls in the area are enhanced when the southward surface current in the HF radar observation area is enhanced. The JCOPE data from 2003 to 2005 was also analyzed, although the period was different from the HF radar observation periods. The beginning of the southward current observed by the HF radar was inferred from the JCOPE data. The time-averaged surface currents to the east of the Kuroshio seem to be bifurcations from the Kuroshio, and are shown to flow southward in the JCOPE data. The southward current flows into the HF radar observation area. The currents are called the Kuroshio southward recirculation current.

[61] The wind stress curl is positive in the eastern part of the Kuroshio, and negative to the east of the Kuroshio, where the Kuroshio seems to be bifurcated in the JCOPE data. The Kuroshio southward recirculation current is sometimes enhanced, when the positive and negative wind stress curls in the area are enhanced as well.

[62] The path of the Kuroshio southward recirculation current is similar to the H contour, which shows that the current is controlled by the bottom topography. The result that enhancement of the southward recirculation current is related with the wind stress curl shows that the wind field is
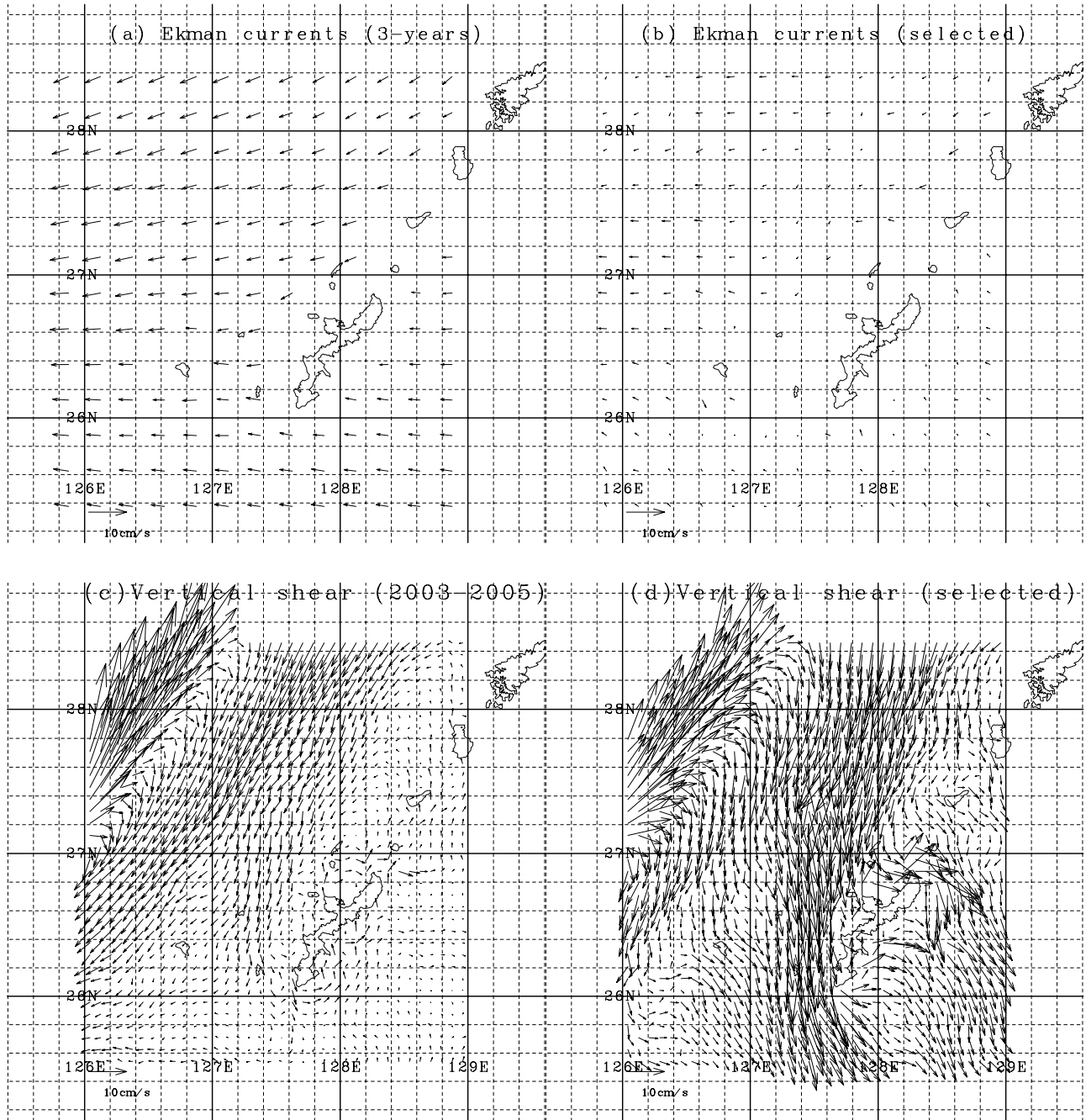
Figure 11. (a) Three-year mean Ekman currents (equation (3)) at $z = -5$ m and (b) same as in Figure 11a but for the selected period. (c) Three-year mean vertical current shears between the surface Ekman layer and the underlying water column and (d) same as in Figure 11c but for the selected period.

also important for the current. Current dynamics will be examined in a future study.

Appendix A: Effective Number of Independent Observations

[63] The expression x_i ($i = 1, \ldots, N$) represents data such as velocity components, and

$$\bar{x} = \frac{1}{N} \sum_i^N x_i \tag{A1}$$

is the sample mean of x_i. The expected value of the population mean (μ) is $\bar{x}$. The confidence interval of the population mean $\Delta_c(\bar{x}, p)$ for the confidence level p is estimated by assuming that the value $X_t = (\bar{x} - \mu)s^{-1}N^{1/2}$ has a Student's t-distribution with $N - 1$ degrees of freedom, where s^2 is the variance estimated from data as

$$S^2 = \frac{1}{N} \sum_i^N (x_i - \bar{x})^2, \tag{A2}$$

$$s^2 = \frac{N}{N-1}S^2. \tag{A3}$$

[64] However, $x_i(i = 1, ., N)$ is the time series data, and the x_i values are not statistically independent of each other. We must use the effective number of independent observations N_e instead of N. The confidence interval of the mean value $\Delta_c(\bar{x}, p)$ for the confidence level p is estimated by assuming that the value $X_t = (\bar{x} - \mu)s^{-1} N_e^{1/2}$ has a Student's t-distribution with $N_e - 1$ degrees of freedom, where s is estimated from (A2) and (A3) by replacing N with N_e in (A3).

[65] The effective number of independent observations N_e is estimated as

$$N_e = \frac{N}{T_d}, \tag{A4}$$

$$T_d = 1 + 2\sum_{l=1}^{N}\left(1 - \frac{l}{N}\right)r_l, \tag{A5}$$

where $r_l(l = 0, ., N)$ is the autocorrelation at lag l [Trenberth, 1984]. The autocorrelation is $r_l = c_l/c_0$ $(l = 0, ., N)$, where c_l is estimated as

$$c_l = \frac{1}{N}\sum_{i=l+1}^{N}(x_{i-l} - \bar{x})(x_i - \bar{x}). \tag{A6}$$

[66] The data of the selected period is not consecutive and (A6) cannot be applied. Suppose that there are J number of samples, such as $M(j)$ observations in each j-th sample ($j = 1, ., J$). The value c_l is estimated by averaging the $c_{l,j}$ as

$$c_{l,j} = \frac{1}{M(j)}\sum_{i=l+1}^{M(j)}(x_{i-l,j} - \bar{x})(x_{i,j} - \bar{x}), \\ l = 1, .., M(j) - 1 \tag{A7}$$

$$\bar{x} = \frac{1}{N}\sum_{j=1}^{J}\sum_{i=1}^{M(j)}x_{i,j} \tag{A8}$$

$$c_l = \sum_{j=1}^{J}\frac{M(j)}{N}c_{l,j}, \tag{A9}$$

where $x_{i,j}(i = 1, ., M(j))$ is the i-th value of j-th sample, and the

$$\sum_{j=1}^{J}M(j) = N \tag{A10}$$

is satisfied. Equations (A7), (A8) and (A9) are identical to (2.14a), (2.14b) and (2.14c) by Trenberth [1984], if $M(j)$ is a constant.

References

Barrick, D. E., M. W. Evans, and B. L. Weber (1977), Ocean surface currents mapped by radar, Science, 198, 138–144.

Bloom, S. C., L. L. Takacs, A. M. da Silva, and D. Ledvina (1996), Data assimilation using incremental analysis updates, Mon. Weather Rev., 124, 1256–1271.

Chelton, D. B., M. G. Schlax, M. H. Freilch, and R. F. Milliff (2004), Satellite measurements reveal persistent small-scale features in ocean winds, Science, 303, 978–983.

Chereskin, T. K. (1995), Direct evidence for an Ekman balance in the California current, J. Geophys. Res., 100, 18,261–18,269.

Collecte Localisation Satellites (2001), SSALTO/DUACS user handbook, report, Toulouse, France.

Guo, X., H. Hukuda, Y. Miyazawa, and T. Yamagata (2003), A triply nested ocean model for simulating the Kuroshio — Roles of horizontal resolution on JEBAR, J. Phys. Oceanogr., 33, 146–169.

Hinata, H., T. Yanagi, T. Takao, and H. Kawamura (2005), Wind-induced Kuroshio warm water intrusion into Sagami Bay, J. Geophys. Res., 110, C03023, doi:10.1029/2004JC002300.

Hisaki, Y. (1996), Nonlinear inversion of the integral equation to estimate ocean wave spectra from HF radar, Radio Sci., 31, 25–39.

Hisaki, Y. (2002), Short-wave directional properties in the vicinity of atmospheric and oceanic fronts, J. Geophys. Res., 107(C11), 3188, doi:10.1029/2001JC000912.

Hisaki, Y. (2004), Short-wave directional distribution for first-order Bragg echoes from the HF ocean radars, J. Atmos. Oceanic Technol., 21, 105–121.

Hisaki, Y. (2005), Ocean wave directional spectra estimation from an HF ocean radar with a single antenna array: Observation, J. Geophys. Res., 110, C11004, doi:10.1029/2005JC002881.

Hisaki, Y. (2006), Ocean wave directional spectra estimation from an HF ocean radar with a single antenna array: Methodology, J. Atmos. Oceanic Technol., 23, 263–286.

Hisaki, Y., and T. Naruke (2003), Horizontal variability of near-inertial oscillations associated with the passage of a typhoon, J. Geophys. Res., 108(C12), 3382, doi:10.1029/2002JC001683.

Hisaki, Y., W. Fujiie, T. Tokeshi, K. Sato, and S. Fujii (2001), Surface current variability east of Okinawa Island obtained from remotely sensed and in situ observational data, J. Geophys. Res., 106, 31,057–31,073.

Kelly, K. A. (1989), An inverse model for near-surface velocity from infrared images, J. Phys. Oceanogr., 19, 1845–1864.

Liu, Y., and Y. Yuan (1999), Variability of the Kuroshio in the East China Sea in 1992, Haiyang Xuebao (Zhongwenban), 18, 1–15.

Marmorino, G., C. L. Trump, F. Askari, N. Allan, D. B. Trizna, and L. K. Shay (1998), An occluded coastal oceanic front, J. Geophys. Res., 103, 21,587–21,600.

Miyazawa, Y., and T. Yamagata (2003), The JCOPE ocean forecast system (in Japanese), Kaiyo Mon., 12, 881–886.

Miyazawa, Y., X. Guo, and T. Yamagata (2004), Roles of meso-scale eddies in the Kuroshio paths, J. Phys. Oceanogr., 34, 2203–2222.

Nadaoka, K., et al. (2001), Regional variation of water temperature around Okinawa coasts and its relationship to offshore thermal environments and coral bleaching, Coral Reefs, 20, 373–384.

Nitani, H. (1972), Beginning of the Kuroshio, in The Kuroshio — Its Physical Aspects, edited by H. Stommel and K. Yoshida, pp. 129–163, Univ. of Tokyo Press, Tokyo.

Oka, E., and M. Kawabe (1998), Characteristics of variations of water properties and density structure around the Kuroshio in the East China Sea, J. Oceanogr., 54, 605–617.

Prandle, D., and D. K. Ryder (1985), Measurement of surface currents in Liverpool Bay by high frequency radar, Nature, 315, 128–131.

Qiu, B., and N. Imasato (1990), A numerical study on the formation of the Kuroshio Counter Current and the Kuroshio Branch Current in the East China Sea, Cont. Shelf Res., 10, 165–184.

Shibata, A., K. Imaoka, M. Kachi, and H. Murakami (1999), SST observation by TRMM microwave imager aboard tropical rainfall mission (in Japanese), Umi no Kenkyu, 8, 135–139.

Takeoka, H., Y. Tanaka, Y. Ohno, Y. Hisaki, A. Nadai, and H. Kuroiwa (1995), Observation of the Kyucho in the Bungo Channel by HF radar, *J. Oceanogr.*, *51*, 699–711.

Trenberth, K. E. (1984), Some effects of finite sample size and persistence on meteorological statistics. Part I: Autocorrelations, *Mon. Weather Rev.*, *112*, 2359–2368.

Xie, S., J. Hafner, Y. Tanimoto, W. T. Liu, H. Tokinaga, and H. Xu (2002), Bathymetric effect on the winter sea surface temperature and climate of the Yellow and East China Seas, *Geophys. Res. Lett.*, *29*(24), 2228, doi:10.1029/2002GL015884.

Yanagi, T., T. Tokeshi, and S. Kakuma (2002), Eddy activities around the Nansei Shoto (Okinawa Islands) revealed by TRMM, *J. Oceanogr.*, *58*, 617–624.

Yuan, Y., K. Takano, Z. Pan, J. Su, K. Kawatate, S. Imawaki, H. Yu, H. Chen, H. Ichikawa, and S. Umatani (1994), The Kuroshio in the East China Sea and the currents east of Ryukyu Islands during autumn 1991, *Mer*, *32*, 235–244.

Zavialov, P. O., R. D. Ghisolfi, and C. A. E. Garcia (2005), An inverse model for seasonal circulation over the Southern Brazilian Shelf: Near-surface velocity from the heat budget, *J. Phys. Oceanogr.*, *28*, 545–562.

———————————

Y. Hisaki, Department of Physics and Earth Sciences, University of the Ryukyus, 1 Aza-Senbaru, Nishihara-cho, Nakagami-gun, Okinawa 903-0213, Japan. (hisaki@sci.u-ryukyu.ac.jp)

C. Imadu, Seiki, 265-2 Makieya-Cho, Nakagyou-ku, Kyoto, Kyoto 604-0857, Japan.